INORGANIC CHEMISTRY FRONTIERS

RESEARCH ARTICLE

View Article Online
View Journal | View Issue

Cite this: *Inorg. Chem. Front.*, 2024, **11**, 3316

Radiochromic semiconductive MOFs with high sensitivity and fast photochromic responses for dual-mode X-ray direct detection†

Xu-Ying Yu,[a,b] Jia-Rong Mi,[a] Qiu-Pei Qin,[a,c] Xin-Ping Fang,[a,c] Yong-Fang Han,[d] Li-Zhen Cai,[a] Ming-Sheng Wang *[a] and Guo-Cong Guo*[a]

Received 26th March 2024,
Accepted 16th April 2024

DOI: 10.1039/d4qi00771a

rsc.li/frontiers-inorganic

X-ray direct detectors, which may directly convert X-rays into electrical signals through semiconductors, are highly desirable for early cancer screening and other applications. Prevailing commercial amorphous Se detectors still suffer from low phase instability and low sensitivity, while the emerging perovskite detectors are subjected to low chemical instability despite high sensitivity and low detection limits. This work reports a viologen-templated Dy(III)-based metal–organic framework (MOF) with radiochromic semiconductive properties and high framework thermal (up to approximately 280 °C) and radiation stability. Its single-crystal detector has an exceptional sensitivity (6385 μC Gy^{-1} cm^{-2} at 271 V cm^{-1}) to tungsten anode X-rays compared to amorphous Se (20 μC Gy^{-1} cm^{-2} at −10 000 V cm^{-1}), single-crystal $MAPbI_3$ perovskite (968.9 μC Gy^{-1} cm^{-2} at −10 V cm^{-1}), and other single-crystal or pellet MOF-based direct detectors (20–3500 μC Gy^{-1} cm^{-2}). Moreover, it exhibits a rapid photochromic response within 10 seconds upon X-ray irradiation and can naturally fade for easy reuse. This property offers the convenience of quickly capturing object information through visual inspection and serves as an alternative means of direct detection outside of traditional electrical imaging methods.

Introduction

Early screening and diagnosis of cancer (typically breast cancer) using X-ray detectors are recognized as effective methods to reduce cancer mortality.[1,2] The most used X-ray detectors employ an indirect detection method, where X-rays are converted into visible light by a scintillator and then detected by a photodiode.[3,4] The method of indirect detection is subjected to limited spatial resolution owing to the scattering nature of the triggered luminescence, and thus difficult to find the nidus as soon as possible.[5] A more advanced approach is the use of direct X-ray detectors.[6] This kind of detector can directly convert X-rays into electrical signals and enable simpler system configurations and higher spatial resolution.[7] Amorphous Se (a-Se) detectors are the prevailing commercial direct detectors, which have played a great role in early cancer screening. However, they suffer from low detection sensitivity (20 μC Gy^{-1} cm^{-2} at −10 000 V cm^{-1}) due to weak X-ray absorption capabilities. Additionally, they easily undergo an α → β phase transition above room temperature, resulting in low phase stability.[8] Perovskites are emerging X-ray detection materials featuring high sensitivity and low detection limits.[9–11] However, their low chemical stability and ionic migration issue remain a great challenge.[12,13] Therefore, many efforts have been made to explore new semiconductors with high sensitivity and high stability for direct X-ray detection in the past few years.[14–17]

MOF-based semiconductor detectors have gained significant attention due to their high stability, decent detection sensitivity, and higher structural designability over inorganic semiconductor and hybrid perovskites.[18–21] The Wang group disclosed the first demonstration of hard radiation detection by semiconductive MOFs.[22] A polycrystalline pellet sample of this Tb(III)–benzoquinone MOF had a thermal stability up to 200 °C and an X-ray sensitivity of 23.8 μC Gy^{-1} cm^{-2} under 80 kV_p X-ray exposure, and is competitive with the commercial a-Se detector. Guo, Zheng and coworkers found that a single-crystal detector of a copper(II) MOF[23] displayed a superior sensitivity of 2697.15 μC Gy^{-1} cm^{-2}. In 2022, Han *et al.* reported a viologen-templated zinc-oxalate semiconductive MOF (EV-MOF detector) with the highest X-ray sensitivity (3216 μC Gy^{-1} cm^{-2}

[a]*State Key Laboratory of Structural Chemistry, Fujian Institute of Research on the Structure of Matter, Chinese Academy of Sciences, Fuzhou, Fujian 3500608, P. R. China. E-mail: mswang@fjirsm.ac.cn*
[b]*University of Chinese Academy of Sciences, Beijing 100049, P. R. China*
[c]*College of Chemistry and Materials Science, Fujian Normal University, Fuzhou, Fujian 350007, P. R. China*
[d]*College of Chemistry and Chemical Engineering, Liaocheng University, Liaocheng, Shandong 252000, P. R. China*

†Electronic supplementary information (ESI) available. CCDC 2336472 (**RCS-2**). For ESI and crystallographic data in CIF or other electronic format see DOI: https://doi.org/10.1039/d4qi00771a

at 1339 V cm^{-1}) so far.[24] Interestingly, this kind of semiconductive MOF exhibits not only photoconductance but a clear color change upon X-ray irradiation.[24,25] For instance, the zinc-oxalate MOF showed a remarkable color change from colorless to blue after irradiation. Unlike the traditional silver-halide photographic plates, these materials show a one-step color change without developing, fixing, and drying operation.[26–28] This property offers the convenience of quickly capturing object information through visual inspection and serves as an alternative means of direct detection outside of traditional electrical imaging methods.

Viologen cations are photochromism active[29,30] and have the ability to enhance charge separation and promote conductance.[31,32] Through incorporating them into a metal–carboxylate framework, we obtained a radiochromic semiconductive MOF, $Na_2(EV)_{0.5}[Dy_2(IPA\text{-}SO_3)_4]\cdot H_2O$ (**RCS-2**; IPA-SO_3 = 5-sulfoisophthalate; EV^{2+} = *N*,*N*′-diethyl-4,4′-bipyridinium cation). The **RCS-2** framework can be stable up to approximately 280 °C and has a high radiation stability. Due to high resistivity and an effective atomic number, a single-crystal detector of **RCS-2** gave a sensitivity of 6385 mC Gy^{-1} cm^{-2} at a bias voltage of 30 V, which is the highest value reported so far for MOFs as direct X-ray detection materials. Besides, **RCS-2** also demonstrated a pronounced and fast photochromic response under X-ray irradiation.

Experimental section

Materials and methods

All chemicals purchased from commercially available sources were of AR grade and used without further purification. Water was deionized and distilled before use. The experimental powder X-ray diffraction (PXRD) pattern was acquired at room temperature on a Rigaku Miniflex 600 Desktop X-ray diffractometer (Tokyo, Japan) using Cu-K_α radiation (λ = 1.54056 Å) ranging from 5° to 50°. The simulated PXRD pattern was derived from the Mercury Version 2020.1 software based on the single crystal X-ray diffraction data. The thermogravimetric analysis experiment was conducted on a Mettler TOLEDO simultaneous TGA/DSC apparatus (Zurich, Switzerland) in N_2, heating the sample in an Al_2O_3 crucible at a heating rate of 5 K min^{-1}. Elemental analyses of C, H, and N were performed using an Elementar Vario EL III microanalyzer (Hesse, Germany). Electron absorption spectra were recorded at room temperature on a PerkinElmer Lambda 950 UV/vis/near-infrared (NIR) spectrophotometer (Waltham, USA) equipped with an integrating sphere and $BaSO_4$ as a reference. Electron paramagnetic resonance (EPR) spectra were recorded on a Bruker-BioSpin ER-420 spectrometer (Rheinstetten, Germany) with a 100 kHz magnetic field in the X band at room temperature.

Single-crystal X-ray crystallography

The structural data of **RCS-2** were collected on Rigaku Mercury X-ray single-crystal diffractometer (Japan). The structure was resolved by direct methods and refined by full-matrix least squares fitting on F^2 using the SHELX-2016 software package.[1] All non-hydrogen atoms were refined with anisotropic thermal parameters except for the solvent molecules. The hydrogen atoms on the aromatic rings were located at geometrically calculated positions and refined by riding. The diffused electron densities resulting from these solvent molecules were removed using the SQUEEZE routine of PLATON. CCDC number 2336472† for **RCS-2** contains crystallographic data for this paper.

Synthesis of RCS-2

$Dy(NO_3)_3\cdot 6H_2O$ (23 mg, 0.05 mmol), 5-sulfoisophthalic acid monosodium salt (IPA-SO_3Na) (20 mg, 0.07 mmol), and $EVBr_2$ (10 mg, 0.03 mmol) were dissolved in a mixture of *N*,*N*′-dimethylformamide (DMF; 2.0 mL), water (0.50 mL) and ethanol (0.50 mL). The vessel was sealed, placed into a 20 mL glass bottle, and heated at 90 °C for 72 hours before cooling slowly to room temperature. The samples were subjected to a cleaning process involving the use of acetone followed by thorough drying. Yellow crystals of **RCS-2** were obtained in 96.60% yield based on IPA-SO_3Na. Anal. calcd (%): C 31.43, H 3.70, N 3.03, found (%): C 31.86, H 3.84, N 2.74.

Radiation detection tests

X-ray detection performance tests were performed at room temperature on a self-assembled X-ray detection device with a tungsten target (λ = 0.21 Å). The X-ray tube voltage was set to 50 kV_p. The electrode samples of **RCS-2** were single crystals of 1.107 × 0.093 × 0.082 mm^3 (Fig. S9†), which are attached with silver wires using silver paste. The charge carrier mobility and lifetime product ($\mu\tau$) was extracted from the bias-dependent photocurrent curve by fitting a modified Hecht equation:

$$I = \frac{I_0 \mu\tau V}{L^2}\left[1 - \exp\left(\frac{-L^2}{\mu\tau V}\right)\right]$$

where I_0 is the saturated photocurrent, V is the applied bias, and L is the material thickness.

Results and discussion

Crystal structure and fundamental characterization

A single crystal X-ray diffraction study revealed that **RCS-2** crystallizes in the *C*2/*c* space group. As shown in Fig. 1a, Dy(III) ions exhibit two coordination modes—Dy1 and Dy2 atoms are eight and nine-coordinated, respectively. Subsequently, the formation of Dy_2O_{17} clusters is facilitated by the carboxylate oxygen atoms on the ligand. The ligands coordinate with the Dy_2O_{17} clusters to construct a three-dimensional framework with one-dimensional open channels extending to the *c* direction (Fig. 1b and c; Fig. S1a†). The presence of π–π interactions between two adjacent ligands (centroid-to-centroid separation: 3.52 Å) (Fig. 1d). The EV^{2+} ions have near *trans*- and *cis*-arrangement of the two ethyl groups along the skeleton. The distance of π–π interactions between EV^{2+} and its adjacent ligand is 3.55 Å (Fig. 1e). The lattice solvent molecules in the

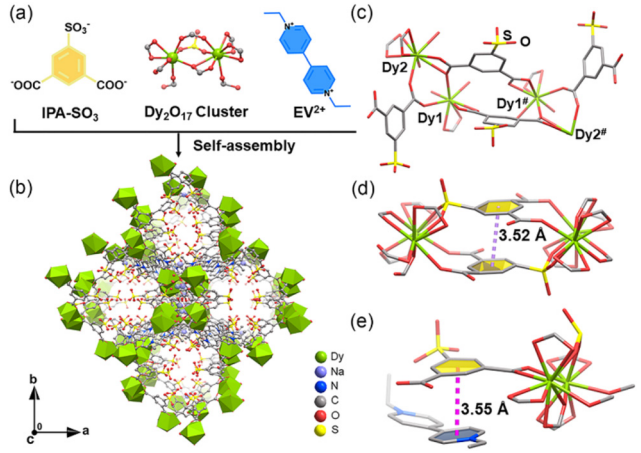

Fig. 1 Crystal structure of **RCS-2**: (a) the main building blocks of the structure. (b) 3D framework viewed along the *c* direction. (c) Coordination spheres of Dy(III) atoms, EV^{2+} and the ligands. (d) and (e) π–π stacking interactions (dashed lines) between the ligand and EV^{2+}. Hydrogen atoms and H_2O molecules are omitted for clarity. Symmetry codes: #1 – *X*, 1 – *Y*, 1 – *Z*.

single crystal structure exhibit a high degree of disorder, necessitating the implementation of SQUEEZE treatment. The transportation of charges is significantly influenced by the chemical structure, in particular, the intermolecular interactions.[33] It is widely recognized that multiple robust π–π interactions in the molecular architecture of materials are advantageous for charge carrier transport. **RCS-2** possesses numerous conjugated π-electron delocalization, mitigates energy losses during the charge transport process and facilitates swift transfer of charge carriers within its structure.

The experimental powder X-ray diffraction (PXRD) patterns (Fig. S2†) indicate that the separated crystalline samples for all tests were pure phase. The structural formula of **RCS-2** was determined through the utilization of thermogravimetric analysis and elemental analysis (Fig. S3†). The thermogravimetric (TGA) analysis reveals that **RCS-2** loses 1.3% of its H_2O molecules first and has no new loss until 280 °C.

Electrical properties upon X-ray irradiation

The performance of an X-ray detector relies not only on its capacity to transmit electrical charges but also on its X-ray absorption efficiency. The atomic composition of the semiconductor plays a crucial role in X-ray detection as it directly influences the X-ray absorption coefficient, which is determined by Z_{eff}^4/E^3 (Z_{eff} is the effective atomic number and E is the X-ray photon energy).[34] It is worth noting that the present **RCS-2** contains Dy, which is a heavy stable element with high X-ray absorption in the periodic table. The Z_{eff} value for **RCS-2** (Z_{eff} is 44.48) is higher than that of a commercial detector a-Se (Z_{eff} is 34). Therefore, **RCS-2** is a highly promising material for high-performance X-ray detectors. Moreover, the simulations of mass attenuation coefficients were investigated across the 1–100 keV range through the XCOM photon section database.[35] This energy range is typical for medical imaging purposes. In Fig. 2b, at a 50 keV photon energy for tungsten anode (W-K_α) X-rays, the mass attenuation coefficient of **RCS-2** is higher than that of EV-MOF, slightly lower than that of the $MAPbI_3$ perovskite, and comparable to that of the a-Se detector. It should be noted that **RCS-2** exhibits a higher absorption coefficient, which improves the X-ray absorption efficiency and, in turn, improves responsiveness to X-rays.

The X-ray detection performance of **RCS-2** was further evaluated in consideration of its good X-ray absorption ability. The initial step involved the preparation of a single crystal X-ray detector device with an Ag/sample/Ag structure,[36] and a schematic diagram is presented in Fig. 2a. Additionally, we conducted a detailed analysis of the optoelectronic characteristics of **RCS-2**. The current–voltage (*I–V*) curve obtained in the absence of light for **RCS-2** exhibited a symmetrical linear relationship in the voltage range from −30 to +30 V, indicating the establishment of an ohmic contact (Fig. 2c). Consequently, the conductivity of **RCS-2** primarily relies on intrinsic carriers generated through thermal excitation rather than injected carriers from an electrical contact. The intrinsic resistivity of **RCS-2** was carefully measured and found to be 4.31×10^8 Ω cm, ensuring minimal leakage current. This low leakage current is a crucial attribute that contributes to achieving a high signal-to-noise ratio in X-ray detection applications. When the **RCS-2** detector was exposed to a W-K_α X-ray at a bias voltage of 30 V (271 V cm^{-1}), it exhibited a distinct photocurrent response. Notably, the intensity of the photocurrent increased in correlation with higher dose rates, indicating that high dose rate X-rays effectively enhanced the concentration of charge carriers, resulting in a greater photocurrent.

To evaluate the comprehensive performance of a material in terms of electronic transport and carrier lifetime, we conducted tests on the carrier mobility–lifetime product ($\mu\tau$), which is one of the important physical parameters in semiconductor materials.[37] A larger $\mu\tau$ value typically indicates better electronic transport characteristics and longer carrier lifetimes, which are crucial for achieving high-performance semiconductor devices. We obtained a $\mu\tau$ value of 1.61×10^{-4} cm^2 V^{-1} for the **RCS-2** detector using a modified Hecht equation, which is comparable to the values observed in perovskite single crystals (10^{-7} to 10^{-2} cm^2 V^{-1} level) and higher than that of a commercial a-Se detector (10^{-7} cm^2 V^{-1} level) (Fig. 2d).

Sensitivity (S) is an essential parameter for direct detectors, as it represents the efficiency of converting incident X-ray photons into collected charges.[38] The S of an X-ray direct detector is defined as the collected charge per unit area per unit of radiation expose. A higher sensitivity enables better imaging contrast while using lower incident dosages, reducing the potential cancer risk for patients during X-ray inspections. To evaluate the sensitivity, we measure the on/off photocurrent response under different dose rates (Fig. S4†). The S value of **RCS-2** is 6385 μC Gy^{-1} cm^{-2} at a bias voltage of 30 V (271 V cm^{-1}) and under a tube voltage 50 kV_p (Fig. 2e). This value upon W-K_α X-ray is higher than that of a-Se (20 μC Gy^{-1} cm^{-2} at −10 000 V cm^{-1}),[8] and other single-crystal or pellet MOF-based direct detectors (20–3500 μC Gy^{-1} cm^{-2})[39] (Table S2†).

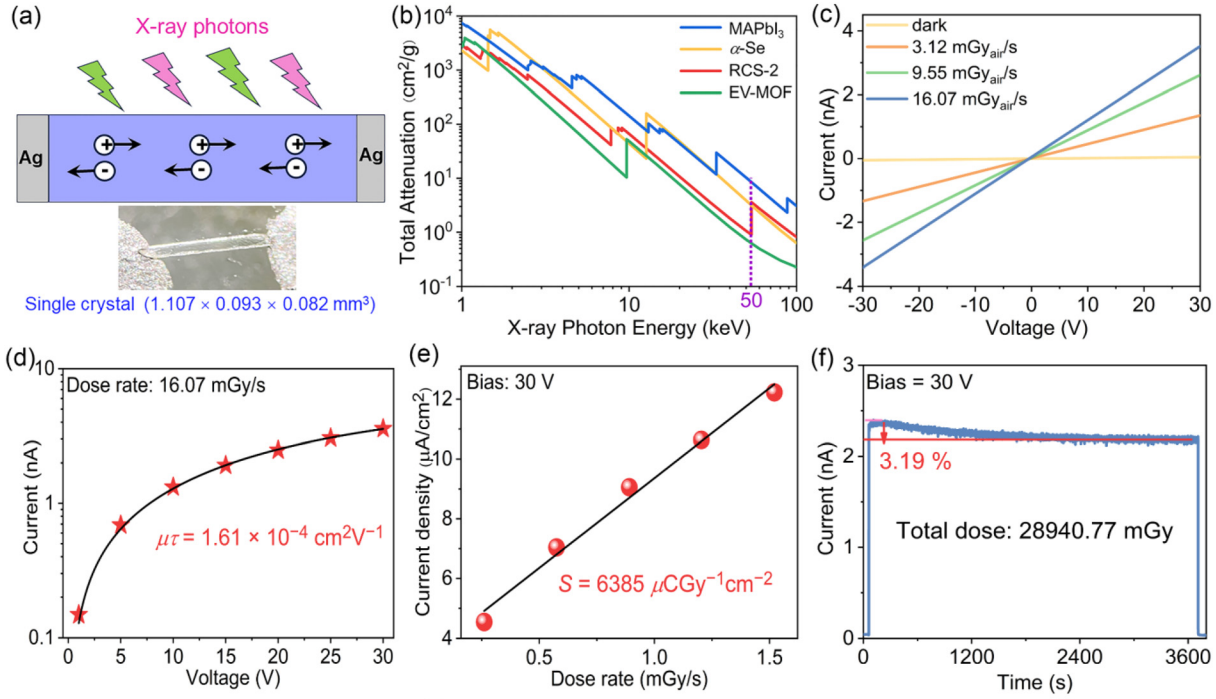

Fig. 2 Single-crystal X-ray detection performance of **RCS-2**: (a) schematic illustration of the X-ray detector and actual electrode diagram. (b) Calculated mass attenuation coefficients. (c) *I*–*V* curves under X-ray off and on with different exposed dose rates. (d) Voltage-dependent photocurrent curves fitted by the Hecht equation. (e) Photocurrent density *versus* dose rate measured at a bias voltage of 30 V. (f) Device stability in air under continuous X-ray irradiation.

Moreover, the response of the detector to X-ray displays a rise time of 125 ms and a decay time of 125 ms at a dose rate of 16.07 mGy s^{-1} (Fig. S5†).

The operational stability and radiation stability are crucial for the application of X-ray detectors. Considering the superior detection performance of the **RCS-2** detector, we investigated its long-term optoelectrical stability under X-ray irradiation. By cyclically turning the X-ray on and off, we recorded the photocurrent curves of the detector at different biases from 1 V to 30 V. The photocurrent remained virtually unchanged after 5 cycles, indicating that the **RCS-2** detector exhibits good operational stability at different biases (Fig. S6†). Additionally, we subjected the material to X-ray irradiation with a dose rate of 7.93 mGy s^{-1}, accumulating a total dose of approximately 28 940.77 mGy over 3600 seconds, which is equivalent to 30 000 commercial X-ray chest radiographs (Fig. 2f). We found that the photocurrent only decreased by 3.19%. This level of decrease is reasonable for a single-crystal X-ray detector, demonstrating its excellent radiation stability. The **RCS-2** detector was thus chosen for X-ray detection because of its high X-ray absorption capability, high $\mu\tau$ product, extremely low dark current, and good environmental stability.

Radiochromism

RCS-2 exhibits noticeable color changes under X-ray irradiation. Cu-K_α (λ = 1.54056 Å) X-rays from a Rigaku FR-X Microfocus single-crystal X-ray diffractometer powered at 2.97 kW and Al-K_α (λ = 0.71073 Å) X-rays from a Thermo Fisher ESCALAB250 X-ray photoelectron spectrometer powered at 150 W were used to investigate the radiochromic properties of **RCS-2**. Under Cu-K_α X-ray irradiation, a visible blue color appeared within 10 seconds, and the color deepened with increasing irradiation time (Fig. 3a and b). Similarly, a similar phenomenon occurred after Al-K_α X-ray irradiation (Fig. S7†). The blue sample displayed absorption bands at approximately 450 and 610 nm [40] (Fig. 4a and Fig. S8†), which is consistent with the characteristic absorption spectrum of viologen monoradicals.[41] A sharp single-line signal at 3515 Gauss (g = 2.000, linewidth = 15 Gauss) in the electron paramagnetic resonance (EPR) spectrum also confirmed the generation of radicals after X-ray-induced coloration (Fig. 4b). Therefore, upon X-ray irradiation, the EV^{2+} cation received the electron and generated the $EV^{\bullet+}$ radical. Consistent with previous reports,[42,43] considering that the closest distances of N···O between the bipyridyl skeleton and IPA-SO_3 ligands are 3.36 Å and 3.85 Å, the O6 and O18 atoms on the carboxyl group of IPA-SO_3 ligands tend to donate electrons and N1 tends to receive electrons during the coloration process (Fig. S1b† and Fig. 4c).

Interestingly, when the X-ray light source was removed, the crystal immediately began to gradually fade, exhibiting visible fading within 10 seconds. There is no structural change observed before and after X-ray irradiation, which can be confirmed by XRD analysis. The fading of **RCS-2** does not require traditional heating methods but can naturally occur when placed in ambient air. This response speed is superior to those of most radiochromic materials reported to date. Furthermore,

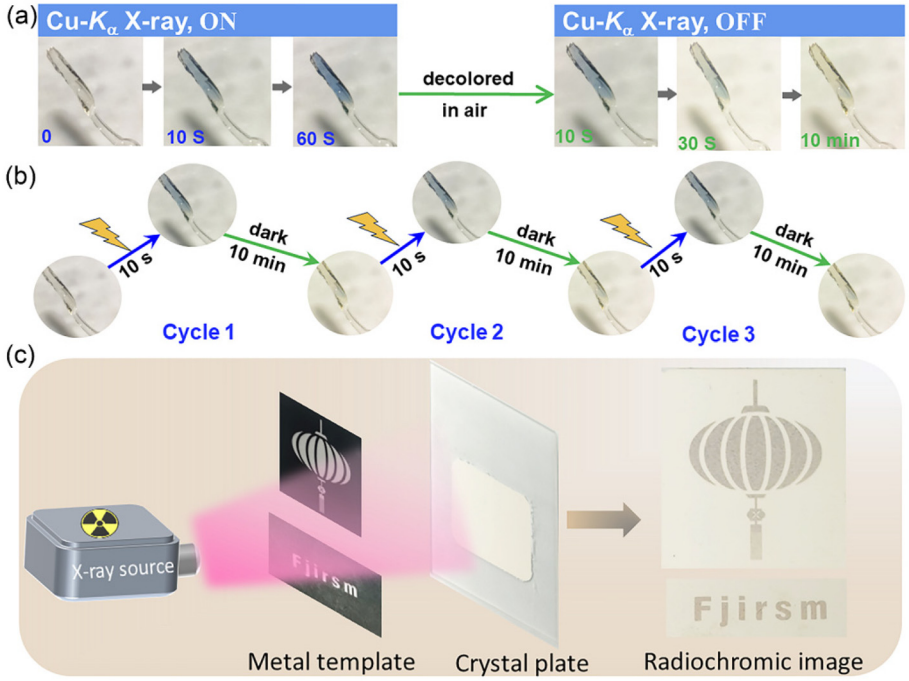

Fig. 3 Radiochromic behavior for **RCS-2**: (a) time-dependent images for crystalline samples of **RCS-2** upon irradiation of Cu-K_α X-rays. (b) Colored–decolored cycles of a single-crystal sample upon irradiation of Cu-K_α. (c) Radiochromism imaging. (The photographs of (a) and (b) were both captured in their original context.)

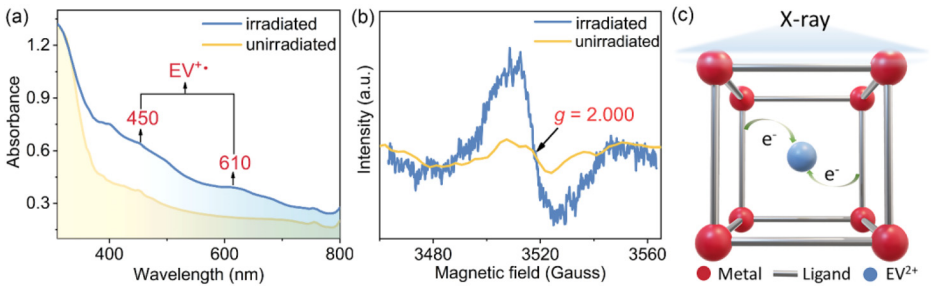

Fig. 4 Radiochromic mechanism for **RCS-2**: (a) electronic absorption spectra before and after irradiation. (b) EPR spectra before and after irradiation. (c) Schematic diagram of the electron transfer mechanism.

the radiochromic performance of **RCS-2** is reversible. After the crystal fades, it can be subjected to irradiation again, resulting in further coloration.

The radiochromic behavior of **RCS-2** enables it to possess radiation imaging capability. A crystal plate was made to serve as a radiation base, and a metal plate was selected as the imaging object. As illustrated in Fig. 3c, the blue pattern appeared on the plate surface, when Cu-K_α X-rays from a powder X-ray diffractometer (power: 600 W) irradiated the colorless crystal plate covered with the printed circuit board for 60 min.

Conclusions

In summary, by incorporating a photochromism-active viologen unit into a metal–carboxylate framework, this study prepared a single-crystal radiochromic semiconductor. Its single-crystal detector has an exceptional sensitivity (6385 μC Gy^{-1} cm^{-2}) to tungsten anode X-rays compared to amorphous Se, single-crystal $MAPbI_3$ perovskite, and other single-crystal or pellet MOF-based direct detectors. Additionally, it exhibits a rapid photochromic response within 10 seconds upon X-ray irradiation and can naturally fade for easy reuse, providing visual detection capability along with electrical signal generation.

Author contributions

Ming-Sheng Wang and Guo-Cong Guo proposed the ideas and supervised the project. Xu-Ying Yu synthesized **RCS-2** and conducted its characterization. Jia-Rong Mi and Li-Zhen Cai per-

formed electrical tests. Qiu-Pei Qin, Xin-Ping Fang and Yong-Fang Han conducted data processing and analysis. Ming-Sheng Wang and Xu-Ying Yu analyzed the data and wrote the manuscript. All authors discussed the results and commented on the manuscript.

Conflicts of interest

The authors declare that they have no known competing financial interest or personal relationships that could have appeared to influence the work reported in this paper.

Acknowledgements

We gratefully acknowledge the financial support by the National Natural Science Foundation (22073102 and 22371279) of China and the National Key Research and Development Program of Ministry of Science and Technology (2021YFB3801604). The authors sincerely thank Prof. Da-Qiang Yuan and Prof. Shao-Fan Wu from Fujian Institute of Research on the Structure of Matter, Chinese Academy of Sciences, for help in crystal analysis and photocurrent upon X-ray irradiation measurements.

Notes and references

1 M. L. Giger, M. F. Inciardi, A. Edwards, J. Papaioannou, K. Drukker, Y. Jiang, R. Brem and J. B. Brown, Automated Breast Ultrasound in Breast Cancer Screening of Women With Dense Breasts: Reader Study of Mammography-Negative and Mammography-Positive Cancers, *Am. J. Roentgenol.*, 2016, **206**, 1341–1350.

2 L. He, Y. Lu, C. Li, H. Xie, J. Zhao, Y. Wang, L. Wang, X. Wang, W. Wang, D. Chen, Y. Gao, B. Li and Y.-F. Li, Non-Targeted Metallomics through Synchrotron Radiation X-ray Fluorescence with Machine Learning for Cancer Screening using Blood Samples, *Talanta*, 2022, **245**, 123486.

3 J.-W. Yuan, Q.-C. Peng, J.-C. Fu, Q. Yang, Z.-Y. Gao, Z.-Y. Wang, K. Li, S.-Q. Zang and B. Z. Tang, Highly Efficient Stable Luminescent Radical-Based X-ray Scintillator, *J. Am. Chem. Soc.*, 2023, **145**, 27095–27102.

4 Q. C. Peng, Y. B. Si, J. W. Yuan, Q. Yang, Z. Y. Gao, Y. Y. Liu, Z. Y. Wang, K. Li, S. Q. Zang and B. Zhong Tang, High Performance Dynamic X-ray Flexible Imaging Realized Using a Copper Iodide Cluster-Based MOF Microcrystal Scintillator, *Angew. Chem., Int. Ed.*, 2023, **62**, e202308194.

5 S. Shi, H. Yao, D. Chen, Z. Li, Z. Xu and Q. Wang, $CsPbX_3$ Based X-Ray Detectors, *Adv. Opt. Mater.*, 2023, **11**, 2300795.

6 C. Liang, S. Zhang, L. Cheng, J. Xie, F. Zhai, Y. He, Y. Wang, Z. Chai and S. Wang, Thermoplastic Membranes Incorporating Semiconductive Metal-Organic Frameworks: An Advance on Flexible X-ray Detectors, *Angew. Chem., Int. Ed.*, 2020, **59**, 11856–11860.

7 X. Geng, Y. A. Chen, Y. Y. Li, J. Ren, G. H. Dun, K. Qin, Z. Lin, J. Peng, H. Tian, Y. Yang, D. Xie and T. L. Ren, Lead-Free Halide Perovskites for Direct X-Ray Detectors, *Adv. Sci.*, 2023, **11**, e2300256.

8 H. Huang and S. Abbaszadeh, Recent Developments of Amorphous Selenium-Based X-Ray Detectors: A Review, *IEEE Sens. J.*, 2020, **20**, 1694–1704.

9 X. He, Y. Deng, D. Ouyang, N. Zhang, J. Wang, A. A. Murthy, I. Spanopoulos, S. M. Islam, Q. Tu, G. Xing, Y. Li, V. P. Dravid and T. Zhai, Recent Development of Halide Perovskite Materials and Devices for Ionizing Radiation Detection, *Chem. Rev.*, 2023, **123**, 1207–1261.

10 J. Jiang, M. Xiong, K. Fan, C. Bao, D. Xin, Z. Pan, L. Fei, H. Huang, L. Zhou, K. Yao, X. Zheng, L. Shen and F. Gao, Synergistic Strain Engineering of Perovskite Single Crystals for Highly Stable and Sensitive X-ray Detectors with Low-Bias Imaging and Monitoring, *Nat. Photonics*, 2022, **16**, 575–581.

11 J. Zhao, L. Zhao, Y. Deng, X. Xiao, Z. Ni, S. Xu and J. Huang, Perovskite-filled membranes for flexible and large-area direct-conversion X-ray detector arrays, *Nat. Photonics*, 2020, **14**, 612–617.

12 K. Sakhatskyi, B. Turedi, G. J. Matt, E. Wu, A. Sakhatska, V. Bartosh, M. N. Lintangpradipto, R. Naphade, I. Shorubalko, O. F. Mohammed, S. Yakunin, O. M. Bakr and M. V. Kovalenko, Stable perovskite single-crystal X-ray imaging detectors with single-photon sensitivity, *Nat. Photonics*, 2023, **17**, 510–517.

13 Z. Li, G. Peng, Z. Li, Y. Xu, T. Wang, H. Wang, Z. Liu, G. Wang, L. Ding and Z. Jin, Hydrogen Bonds Strengthened Metal-Free Perovskite for Degradable X-ray Detector with Enhanced Stability, Flexibility and Sensitivity, *Angew. Chem., Int. Ed.*, 2023, **62**, e202218349.

14 R. Shi, J. Pi, D. Chu, B. Jia, Z. Zhao, J. Hao, X. Zhang, X. Dong, Y. Liang, Y. Zhang, Y. Liu and S. Liu, Promoting Band Splitting through Symmetry Breaking in Inorganic Halide Perovskite Single Crystals for High-Sensitivity X-ray Detection, *ACS Energy Lett.*, 2023, **8**, 4836–4847.

15 Y. Song, L. Li, M. Hao, W. Bi, A. Wang, Y. Kang, H. Li, X. Li, Y. Fang, D. Yang and Q. Dong, Elimination of Interfacial-Electrochemical-Reaction-Induced Polarization in Perovskite Single Crystals for Ultrasensitive and Stable X-Ray Detector Arrays, *Adv. Mater.*, 2021, **33**, 2103078.

16 M. Zhang, C. Liang, G.-D. Cheng, J. Chen, Y. Wang, L. He, L. Cheng, S. Gong, D. Zhang, J. Li, S.-X. Hu, D. Juan, G. Wu, Y. Wang, Z. Chai and S. Wang, Intrinsic Semiconducting Behavior in a Large Mixed-Valent Uranium(V/VI) Cluster, *Angew. Chem., Int. Ed.*, 2021, **60**, 9886–9890.

17 H. Lu, J. Xie, X.-Y. Wang, Y. Wang, Z.-J. Li, K. Diefenbach, Q.-J. Pan, Y. Qian, J.-Q. Wang, S. Wang and J. Lin, Visible colorimetric dosimetry of UV and ionizing radiations by a dual-module photochromic nanocluster, *Nat. Commun.*, 2021, **12**, 2798.

18 C. Liang, L. Cheng, S. Zhang, S. Yang, W. Liu, J. Xie, M. D. Li, Z. Chai, Y. Wang and S. Wang, Boosting the

Optoelectronic Performance by Regulating Exciton Behaviors in a Porous Semiconductive Metal-Organic Framework, *J. Am. Chem. Soc.*, 2022, **144**, 2189–2196.

19 X. Zhang, H. Qiu, W. Luo, K. Huang, Y. Chen, J. Zhang, B. Wang, D. Peng, Y. Wang and K. Zheng, High-Performance X-Ray Imaging using Lanthanide Metal-Organic Frameworks, *Adv. Sci.*, 2023, **10**, e2207004.

20 B. Chen, J. Wang, L. Peng, Q. Wang, Y. Wang and X. Xu, Radiation–Responsive Metal–Organic Frameworks: Fundamentals and Applications, *Adv. Funct. Mater.*, 2023, **34**, 2310270.

21 Y. Zhang, X. Wang, K. Xu, F. Zhai, J. Shu, Y. Tao, J. Wang, L. Jiang, L. Yang, Y. Wang, W. Liu, J. Su, Z. Chai and S. Wang, Near-Unity Energy Transfer from Uranyl to Europium in a Heterobimetallic Organic Framework with Record-Breaking Quantum Yield, *J. Am. Chem. Soc.*, 2023, **145**, 13161–13168.

22 Y. Wang, X. Liu, X. Li, F. Zhai, S. Yan, N. Liu, Z. Chai, Y. Xu, X. Ouyang and S. Wang, Direct Radiation Detection by a Semiconductive Metal–Organic Framework, *J. Am. Chem. Soc.*, 2019, **141**, 8030–8034.

23 B.-Y. Li, M.-J. Xie, J. Lu, W.-F. Wang, R. Li, J.-R. Mi, S.-H. Wang, F.-K. Zheng and G.-C. Guo, Highly Sensitive Direct X-Ray Detector Based on Copper(II) Coordination Polymer Single Crystal with Anisotropic Charge Transport, *Small*, 2023, **19**, 2302492.

24 Y.-F. Han, X.-M. Xu, S.-H. Wang, W.-F. Wang, M.-S. Wang and G.-C. Guo, Reusable radiochromic semiconductive MOF for dual-mode X-ray detection using color change and electric signal, *Chem. Eng. J.*, 2022, **437**, 135468.

25 X. Yu, J. Mi, Y. Han, C. Sun, M. Wang and G. Guo, A stable radiochromic semiconductive viologen-based metal–organic framework for dual-mode direct X-ray detection, *Chin. Chem. Lett.*, 2023, DOI: **10.1016/j.cclet.2023.109233**.

26 M.-S. Wang, C. Yang, G.-E. Wang, G. Xu, X.-Y. Lv, Z.-N. Xu, R.-G. Lin, L.-Z. Cai and G.-C. Guo, A Room-Temperature X-ray-Induced Photochromic Material for X-ray Detection, *Angew. Chem., Int. Ed.*, 2012, **51**, 3432–3435.

27 P. Y. Guo, C. Sun, N. N. Zhang, L. Z. Cai, M. S. Wang and G. C. Guo, An Inorganic-Organic Hybrid Photochromic Material with Fast Response to Hard and Soft X-rays at Room Temperature, *Chem. Commun.*, 2018, **54**, 4525–4528.

28 Y. B. Su, Y. Q. Wei, L. Z. Cai, P. X. Li, M. S. Wang and G. C. Guo, Energy-Dependent Photochromism at Room Temperature for Visually Detecting and Distinguishing X-rays, *Chem. Commun.*, 2018, **54**, 12349–12352.

29 L. Liu, Q. Liu, R. Li, M. S. Wang and G. C. Guo, Controlled Photoinduced Generation of "Visual" Partially and Fully Charge Separated States in Viologen Analogues, *J. Am. Chem. Soc.*, 2021, **143**, 2232–2238.

30 P. H. Wang, C. M. Yu, X. Q. Yu, M. S. Wang and G. C. Guo, UV-vis/X-ray/Thermo-Induced Synthesis and UV-SWIR Photoresponsive Property of a Mixed-Valence Viologen Molybdate Semiconductor, *Chem. Commun.*, 2021, **57**, 5550–5553.

31 C. Sun, X. Q. Yu, M. S. Wang and G. C. Guo, A Smart Photochromic Semiconductor: Breaking the Intrinsic Positive Relation Between Conductance and Temperature, *Angew. Chem., Int. Ed.*, 2019, **58**, 9475–9478.

32 C. Sun, M. S. Wang and G. C. Guo, Covalently Bonded Pillared Layered Bromoplumbate with High Thermal Stability: High Capacitance Gain after Photoinduced Electron Transfer, *ACS Appl. Mater. Interfaces*, 2019, **11**, 30713–30718.

33 L. S. Xie, G. Skorupskii and M. Dinca, Electrically Conductive Metal-Organic Frameworks, *Chem. Rev.*, 2020, **120**, 8536–8580.

34 M.-J. Xie, J. Lu, B.-Y. Li, W.-F. Wang, S.-H. Wang, F.-K. Zheng and G.-C. Guo, Barium(II)-Based Semiconductive Coordination Polymers for High-Performance Direct X-ray Detection and Imaging: Reducing the Exciton Binding Energy Via Enhancing π-π Interactions, *Chem. Eng. J.*, 2023, **466**, 143272.

35 L. Cheng, C. Liang, W. Liu, Y. Wang, B. Chen, H. Zhang, Y. Wang, Z. Chai and S. Wang, Three-Dimensional Polycatenation of a Uranium-Based Metal-Organic Cage: Structural Complexity and Radiation Detection, *J. Am. Chem. Soc.*, 2020, **142**, 16218–16222.

36 L. Sun, S. S. Park, D. Sheberla and M. Dinca, Measuring and Reporting Electrical Conductivity in Metal Organic Frameworks: Cd_2(TTFTB) as a Case Study, *J. Am. Chem. Soc.*, 2016, **138**, 14772–14782.

37 A. Ruzin and Y. Nemirovsky, Methodology for Evaluation of Mobility-lifetime Product by Spectroscopy Measurements in CdZnTe Spectrometers, *J. Appl. Phys.*, 1997, **82**, 4166–4171.

38 Y. Wu, J. Feng, Z. Yang, Y. Liu and S. F. Liu, Halide Perovskite: A Promising Candidate for Next-Generation X-Ray Detectors, *Adv. Sci.*, 2022, **10**, e2205536.

39 H. Chen, J. Chen, M. Li, M. You, Q. Chen, M. Lin and H. Yang, Recent Advances in Metal-Organic Frameworks for X-ray Detection, *Sci. China: Chem.*, 2022, **65**, 2338–2350.

40 P. S. Braterman and J. I. Song, Spectroelectrochemistry of Aromatic Ligands and Their Derivatives. 1. Reduction Products of 4,4′-Bipyridine, 2,2′-Bipyridine, 2,2′-Bipyrimidine, and Some Quaternized Derivatives, *J. Org. Chem.*, 1991, **56**, 4678–4682.

41 Y. Han, N. Zhang, M. Wang and G. Guo, Achieving Different Color Changes for Photochromic Compounds by Controlling Coordination Modes, *J. Phys. Chem. C*, 2020, **124**, 27680–27686.

42 Q.-Y. Pan, M.-E. Sun, C. Zhang, L.-K. Li, H.-L. Liu, K.-J. Li, H.-Y. Li and S.-Q. Zang, A Multi-Responsive Indium-Viologen Hybrid with Ultrafast-Response Photochromism and Electrochromism, *Chem. Commun.*, 2021, **57**, 11394–11397.

43 L. Z. Cai, Z. Z. Yao, S. J. Lin, M. S. Wang and G. C. Guo, Photoinduced Electron-Transfer (PIET) Strategy for Selective Adsorption of CO_2 over C_2H_2 in a MOF, *Angew. Chem., Int. Ed.*, 2021, **60**, 18223–18230.

